The Astrophysical Journal, 913:51 (13pp), 2021 May 20 https://doi.org/10.3847/1538-4357/abef63

Thermonuclear ^{19}F(p, α)^{16}O Reaction Rate Revised and Astrophysical Implications

L. Y. Zhang[1,2], A. Y. López[3], M. Lugaro[3,4,5], J. J. He[1,2], and A. I. Karakas[5,6]
[1] Key Laboratory of Beam Technology of Ministry of Education, College of Nuclear Science and Technology, Beijing Normal University, Beijing 100875, People's Republic of China; hejianjun@bnu.edu.cn
[2] Beijing Radiation Center, Beijing 100875, People's Republic of China
[3] Konkoly Observatory, Research Centre for Astronomy and Earth Sciences, Konkoly Thege Miklós út 15-17, H-1121 Budapest, Hungary; maria.lugaro@csfk.mta.hu
[4] ELTE Eötvös Loránd University, Institute of Physics, Budapest 1117, Pázmány Péter sétány 1/A, Hungary
[5] School of Physics and Astronomy, Monash University, VIC 3800, Australia
[6] ARC Centre of Excellence for All Sky Astrophysics in 3 Dimensions (ASTRO 3D), Australia
Received 2020 October 19; revised 2021 March 8; accepted 2021 March 15; published 2021 May 24

Abstract

We have calculated the thermonuclear ^{19}F(p, α_γ)^{16}O reaction rate in a wide temperature region of 0.001–10 GK by re-evaluating the available experimental data. Together with recently evaluated ^{19}(p, α_0)^{16}O and ^{19}(p, α_π)^{16}O data, we have derived a new total reaction rate of ^{19}F(p, α)^{16}O using a Monte Carlo technique. The present rate is larger than the NACRE recommended one by factors of 36.4, 2.3, and 1.7 at temperatures of 0.01, 0.05, and 0.1 GK, respectively. This is because we have considered the enhanced low-energy astrophysical S factors in the (p, α_γ) channel, owing to the interference effect between an 11 keV resonance and the well-known 323 keV resonance. It shows that the (p, α_γ) channel dominates the total rate over the entire temperature region, except for a narrow region of 0.05–0.12 GK where the (p, α_0) channel dominates, contrary to the previous conclusion. We have investigated the impact of the ^{19}F(p, α)^{16}O reaction rate using a simple parametric model of extra mixing in low-mass AGB stars, which would lower the fluorine abundance produced and observed in these stars. However, models considering different temperature profiles and more sophisticated approaches, such as extra mixing induced by magnetic fields, are needed to verify the results of our preliminary tests. Interestingly, our new rate has a strong impact on destruction of ^{19}F in the CNO cycle at low temperatures of 0.02–0.03 GK, and this general behavior needs to be analyzed further.

Unified Astronomy Thesaurus concepts: Helium burning (716); Reaction rates (2081); S-process (1419); Massive stars (732); Asymptotic giant branch stars (2100); Stellar nucleosynthesis (1616)

1. Introduction

Fluorine is one of the most interesting elements in nuclear astrophysics because the abundance of the only stable fluorine isotope, ^{19}F, is very sensitive to the physical conditions within stars. Therefore, fluorine is often used to probe nucleosynthesis scenarios (Lucatello et al. 2011). Fluorine can be produced during the core collapse of Type II supernovae (Woosley & Haxton 1988) in Wolf–Rayet and fast-rotating massive stars (Meynet & Arnould 2000) and in the convective zones triggered by thermal pulses in asymptotic giant branch (AGB) stars (Cristallo et al. 2009). Pandey et al. (2008) observed fluorine overabundances by factors of 800–8000 in R-Coronae-Borealis stars, providing evidence that fluorine synthesis also occurs in these hydrogen-deficient supergiants. However, in spite of the crucial importance of fluorine nucleosynthesis, a detailed knowledge of all the reaction rates involved in it is still missing (Lugaro et al. 2004; La Cognata et al. 2011, 2015).

AGB stars are one of the major contributors to Galactic fluorine (Jorissen et al. 1992). In these stars, fluorine is produced in the He-rich intershell and carried to the surface via recurrent dredge-up episodes (Lugaro et al. 2004). However, deep mixing phenomena in these AGB stars can alter the stellar surface composition due to proton capture at low temperatures and the transport of material affected by such reactions (Nollett et al. 2003; Busso et al. 2010; Sergi et al. 2010). In this environment, the main fluorine destruction reaction ^{19}F(p, α)^{16}O possibly modifies the surface abundance of fluorine (Abia et al. 2011; Lucatello et al. 2011). As for the hydrogen-deficient post-AGB stars, hydrogen mixing plays a key role together with He burning and helps to produce elemental abundances in better agreement with observations (Clayton et al. 2007). Here, the ^{19}F(p, α)^{16}O reaction also might bear great importance as it would remove both protons and fluorine nuclei from this nucleosynthetic site.

Figure 1 shows the level scheme of the ^{19}F(p, α)^{16}O reaction. It is well-known that this reaction takes place via three different types of channels: (p, α_0), (p, α_π), and (p, α_γ). Hereafter, the group of (p, α_2), (p, α_3), and (p, α_4) accompanying the γ transitions of γ_2, γ_3, and γ_4, is referred to as the (p, α_γ) channel. In general, the (p, α_0) channel dominates at lower temperatures below ~0.15 GK, while about 90% of the contribution is due to the (p, α_γ) channel at temperatures above 0.2 GK (Indelicato et al. 2017; He et al. 2018). The (p, α_π) channel provides at most a ~10% contribution at low temperatures around 0.05 GK (Indelicato et al. 2017). Our new evaluation of the (p, α_γ) rate presented below, however, will result in different contributions of (p, α_0) and (p, α_γ) in the low temperature region of 0.001–0.1 GK.

Most recently, the (p, α_0) and (p, α_π) rates have been calculated based on the re-evaluated experimental data by He et al. (2018) and Lombardo et al. (2019), respectively. As for the (p, α_γ) rate, the Nuclear Astrophysics Compilation of Reaction Rate (NACRE;[7] Angulo et al. 1999) compiled a resonant parameter table for computing the resonant contribution and adopted the experimental astrophysical $S(E)$ factors of Spyrou et al. (1997) for $E_{\mathrm{c.m.}} = 0.957$–3.438 MeV (hereafter,

[7] http://pntpm.ulb.ac.be/Nacre/nacre.htm

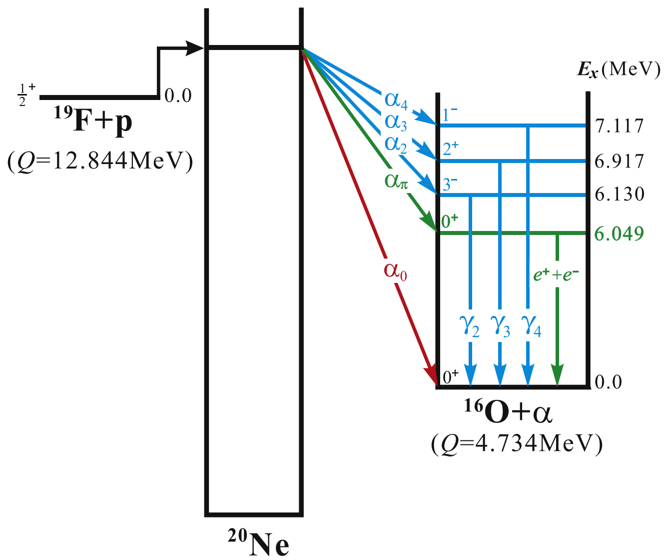

Figure 1. Level scheme of the ^{19}F(p, α)^{16}O reaction.

SP97) and of Willard et al. (1952) for $E_{\rm c.m.} = 3.47–5.15$ MeV (hereafter, WI52). More experimental data available since then still need to be evaluated, especially the direct measurement data of Spyrou et al. (2000; hereafter, SP00). For readers, the corresponding references for the acronyms (e.g., SP97, WI52 and SP00) that are utilized in this work are listed in the Appendix.

In this work, we have re-evaluated the cross-section, astrophysical S factor and the resonant parameters for the ^{19}F(p, α_γ)^{16}O channel in the energy region $E_{\rm c.m.} = 0 \sim 5.2$ MeV. Based on the available experimental data and theoretical low-energy extrapolation, we have calculated the ^{19}F(p, α_γ)^{16}O rate in the temperature region of 0.001–10 GK. Together with the recently re-evaluated (p, α_0) data (He et al. 2018) and (p, α_π) data (Lombardo et al. 2019), we present a new total reaction rate of ^{19}F(p, α)^{16}O. We also show the impact of the present new thermonuclear ^{19}F(p, α)^{16}O rate on the fluorine stellar surface abundance in the scenario of extra mixing in AGB stars.

2. ^{19}F(p, α_γ)^{16}O Data Evaluation

We have separated the ^{19}F(p, α_γ)^{16}O data into three energy regions. Region I is 0 MeV $< E_{\rm c.m.} <$ 0.2 MeV, Region II 0.2 MeV $< E_{\rm c.m.} <$ 3.45 MeV, and Region III is 3.45 MeV $< E_{\rm c.m.} <$ 5.17 MeV.

2.1. Region I: 0 MeV $< E^{\rm c.m.} <$ 0.2 MeV (Figure 2)

After the NACRE compilation, SP00 performed a ^{19}F(p, α_γ)^{16}O direct measurement down to what is so far the lowest energy point ever reached of $E_{\rm c.m.} = 188.8$ keV. By considering the interference effect between the $E_{\rm r}^{\rm c.m.} = 11$ keV and 323 keV resonances, the astrophysical S factors were calculated toward the zero energy region as shown in their Figure 6. Kious (1990) studied the ^{19}F(^{3}He,d)^{20}Ne reaction and found the existence of this 11 keV resonance (i.e., $E_{\rm r}^{\rm lab} = 11.6$ keV listed in Table 1 of SP00), which was assigned as $J^\pi = 1^+$ with a spectroscopic factor of $S_p = 0.056$. This candidate level was also reported by Betts et al. (1975), but situated 25 keV below threshold. SP00 fitted their experimental data by assuming the existence of this resonance, for which a width of $\Gamma = 2–120$ eV was recommended. The lowest χ^2 was achieved for a width of 30 eV. Different possible values of this width introduce large uncertainties to the S factor below $E_p = 200$ keV. For example, the S factor at the 11 keV resonance peak was predicted to be roughly 6×10^4 MeV·b and 2×10^3 MeV·b, by using two different widths of $\Gamma_{E_{\rm r}=11} = 1$ keV and 30 eV, respectively. Owing to this low energy resonance, the S factor of the (p, α_γ) channel is much larger than that of the (p, α_0) channel in the very low energy region, up to 2–3 orders of magnitude when on the resonance. As described in detail below, we have found that the (p, α_γ) channel dominates the total reaction rate in the very low temperature region, over the (p, α_0) channel owing to this low energy resonance. This is almost completely contrary to the previous scenarios of SP00 and Indelicato et al. (2017).

Using a similar analysis and fit method to those described by SP00, we have reanalyzed the low-energy S factor data presented in their Figure 6. However, we cannot reproduce their two S factor curves when using the same resonant parameters listed in their Table 1 and $\ell_{\rm p}$ values allowed for the proton channels. The well-studied 323 keV resonance has a spin-parity of $J^\pi = 1^+$ (Angulo et al. 1999), thus the most probable $\ell_{\rm p}$ values should be either 0 or 2 because $J^\pi = 1/2^+$ for both the proton and the ^{19}F ground state. We can only reproduce the $\Gamma_{E_{\rm r}=11} = 30$ eV curve in Figure 6 of SP00 if we use $\ell_p = 3$ for the 323 keV resonance and we can only reproduce their $\Gamma_{E_{\rm r}=11} = 1$ keV curve if we use $\ell_p = 4$ for both 323 and 564 keV resonances. Therefore, we present a revision of such results as described below and the impact on the final reaction rate. Some more details about this issue can be found in the Appendix.

We have reanalyzed the 12 low-energy data points of SP00 with the same method and resonant parameters, but using the allowed $\ell_{\rm p}$ values as discussed above. Here, the only free fit parameter was the width of the 11 keV resonance. The lowest χ^2 value has been achieved for a value of $\Gamma_{E_{\rm r}=11} = 1587$ eV. Our results are shown in Figure 2(a) by three curves for widths of $\Gamma_{E_{\rm r}=11} = 1587$ eV (best fit), 1305 eV, and 1895 eV. The comparison to the previous results shown in Figure 2(b) demonstrates that the present low-energy S factor curve (red solid line) is dramatically different from those previously recommended (i.e., the black solid and dotted lines). The ^{19}F(p, α_γ)^{16}O rate with the $\Gamma_{E_{\rm r}=11} = 1587$ eV curve, and the ratio relative to that of SP00 $\Gamma_{E_{\rm r}=11} = 30$ eV curve are shown in Figure 3. The width of the 11 keV resonance and its interference effect with the 323 keV resonances affect the reaction rate more significantly at low temperatures than previously thought. Therefore, further experimental verification of the existence of the 11 keV resonance and studies of its properties (such as, $E_{\rm r}$, J^π, and Γ) are strongly required.

2.2. Region II: 0.2 MeV $< E^{\rm c.m.} <$ 3.45 MeV (Figures 2, 4, and 5)

In this region, we separate the traditional narrow resonant contribution from the other contributions. The latter include the non-resonant contribution, and the broad resonances and their tails whose resonant parameters were not fitted before, for which we use here the experimental data listed in Table 3 of SP97.

Table 1
Resonance Strengths of ^{19}F(p, α_γ)^{16}O. Table 5 in the Appendix Lists More Information

	$\omega\gamma$ (eV)					Adopted $\omega\gamma$ (eV)[b]	
$E_r^{c.m.}$ (keV)[a]	SP00	SP97	ZA95a	CR91	BE82	Present	NACRE
11.0 $\pm$ **2.6**[g]	8.5×10^{-29}					$(7.5 \pm 3.0) \times 10^{-29}$	$(7.5 \pm 3.0) \times 10^{-29}$
212.71 $\pm$ 0.07	0.0126 $\pm$ 0.0013					0.0126 $\pm$ 0.0013	0.022 $\pm$ 0.004
225.15 $\pm$ 0.48	0.0011 $\pm$ 0.0004					0.0011 $\pm$ 0.0004	
323.31 $\pm$ 0.04	24.3 $\pm$ 2.9	24.7 $\pm$ 3.1[c]	24.4 $\pm$ 1.3[d]	23.0 $\pm$ 0.8[e]		23.5 $\pm$ 0.6	23.1 $\pm$ 0.9
459.53 $\pm$ 0.09	8 $\pm$ 1					8 $\pm$ 1	9.5 $\pm$ 0.7
564.42 $\pm$ 0.90	48 $\pm$ 7					48 $\pm$ 7	50 $\pm$ 6
635.31 $\pm$ 0.62	75 $\pm$ 9					75 $\pm$ 9	88 $\pm$ 10
790.53 $\pm$ 0.29		17 $\pm$ 5				17 $\pm$ 5	27 $\pm$ 6
828.17 $\pm$ 0.19		760 $\pm$ 70			781 $\pm$ 41[f]	775 $\pm$ 35	785 $\pm$ 32
853.71 $\pm$ 0.71		27 $\pm$ 7				27 $\pm$ 7	29 $\pm$ 3
887.14 $\pm$ 0.49		430 $\pm$ 50				430 $\pm$ 50	452 $\pm$ 31
1032.24 $\pm$ 0.48		7.9 $\pm$ 1.0				7.9 $\pm$ 1.0	6.9 $\pm$ 0.6
1078.77 $\pm$ 0.88		29 $\pm$ 4				29 $\pm$ 4	23 $\pm$ 3
1214.78 $\pm$ 0.48		202 $\pm$ 26				202 $\pm$ 26	225 $\pm$ 24
1276.73 $\pm$ 0.54		280 $\pm$ 70				280 $\pm$ 70	347 $\pm$ 35
1301.90 $\pm$ 0.51		1860 $\pm$ 230				1860 $\pm$ 230	2005 $\pm$ 143
1522.03 $\pm$ 0.55		44 $\pm$ 12				44 $\pm$ 12	44 $\pm$ 12

Notes.
[a] Adopted from NACRE.
[b] Weighted average.
[c] Value from Zahnow et al. (1995) for α_2 group, $\omega\gamma(\alpha_2) = 24 \pm 3$ eV, normalized by the α_2 branching ratio 0.97 of Ajzenberg-Selove (1987).
[d] Value from Croft (1991) for α_2 group, $\omega\gamma(\alpha_2) = 23.7 \pm 1.2$ eV, normalized by the α_2 branching ratio 0.97 of Ajzenberg-Selove (1987).
[e] Value from Becker et al. (1982) for α_2 group, $\omega\gamma(\alpha_2) = 22.3 \pm 0.8$ eV, normalized by the α_2 branching ratio 0.97 of Ajzenberg-Selove (1987).
[f] Value from Becker et al. (1982) for α_2 group, $\omega\gamma(\alpha_2) = 570 \pm 30$ eV, normalized by the α_2 branching ratio 0.73 of Ajzenberg-Selove (1987).
[g] Adopted from Kious (1990).

2.2.1. Traditional Resonant Contribution

We have taken all resonant parameters determined by SP97 and SP00 except for two resonances at $E_r^{c.m.} = 323$ keV and 828 keV. For these two resonances, the present $\omega\gamma$ values are obtained by a weighted average of all listed values which originally had a cited uncertainty. The experimental $\omega\gamma$ values available for the resonances in the ^{19}F(p, α_γ)^{16}O reaction are listed in Table 1. The NACRE adopted values are listed in the last column for comparison.

2.2.2. Other Contributions

The experimental cross-section data available are shown in Figure 4 for comparison. Here, SP97 data are from their Table 3, the same as adopted by NACRE. The data shown in Figure 1 of Ranken et al. (1958; hereafter, RA58) and Figure 3 of Cuzzocrea et al. (1980; hereafter, CU80) were compiled in the Experimental Nuclear Reaction Data (EXFOR) library,[8] which is also shown for comparison. Figure 4 shows that if the RA58 data are multiplied by a factor of 0.7 (filled squares labeled as "RA58 (EXFOR×0.7) in the plot"), then they agree with the SP97 data within the uncertainties above 1.4 MeV. This factor of 0.7 is consistent with that adopted in a recent (p, α_0) evaluation for the RA58 data by He et al. (2018). We speculate that the target thickness in RA58 was underestimated by about 30%. In Figure 4, we show the energy scale as $E_{c.m.} = [E_p - \Delta(E_p)/2] \times \frac{19}{20}$, where E_p is taken from Figure 1 of RA58 and the target thickness effect is considered with an energy loss of $\Delta(E_p) = 30$ keV calculated by a LISE code[9] (Tarasov & Bazin 2004). According to RA58, their 0.22 mg cm^{-2} target thickness of CaF_2 meant a 24 keV energy loss for 2 MeV protons, thus our estimated 30 keV thickness is about 30% thicker than their cited value. This may verify our speculation above. In addition, the relative measurement of RA58 was normalized to a previous measurement of Chao et al. (1950) rather than an absolute measurement and this method may also introduce uncertainties.

As for the CU80 data compiled in the EXFOR library, presently a small target thickness effect of $\Delta \approx 3$ keV, i.e., for their claimed nominal CaF_2 target thickness of $\sim$20 μg cm^{-2} has been considered in Figure 4 to calculate the triangles labeled as "CU80 (Present)". In fact, the summed ($\alpha_1 + \alpha_2 + \alpha_3$) data shown in Figure 3 of CU80 correspond directly to the (p, α_γ) cross sections. CU80 shows a resonance peak at 1.621 MeV, about 20 keV higher than that of SP97, which indicates that their target thickness should be about $\Delta \approx 40$ keV (i.e., a CaF_2 thickness of $\sim$300 μg cm^{-2} v their nominal value of $\sim$20 μg cm^{-2}), if their proton beam calibration was correct. In addition, locations of other high-energy resonances of CU80 deviate significantly from those of SP97. We cannot speculate the exact reason for this deviation, but one possibility is carbon deposition on the target surface during bombardment, as we observed recently (Zhang et al. 2019). Because of the significant deviation discussed above, the CU80 data are not included in the present evaluation.

Figure 5 shows an expansion of Figure 4 for the low-energy region including two more data sets, the cross sections σ_R and errors for five resonances listed in Table 2 of SP97, and the cross sections derived based on the yield curve as shown in Figure 5 of SP97. Here, we obtained the yields (y) by digitizing the curve in Figure 5 of SP97, and then converted them to the

[8] https://www.nndc.bnl.gov/exfor/exfor.htm
[9] LISE, http://lise.nscl.msu.edu/.

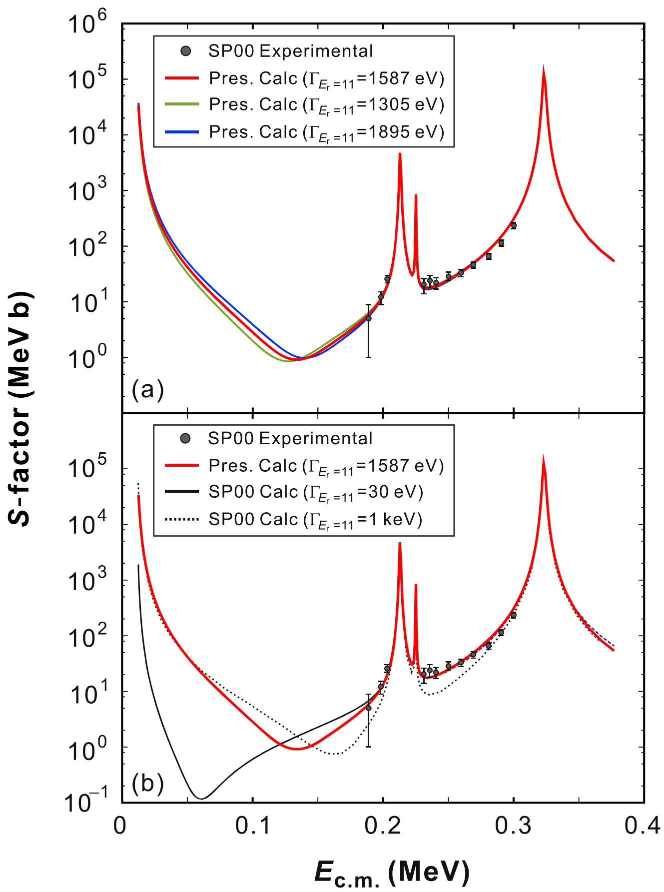

Figure 2. Experimental and calculated S-factors for low-energy ^{19}F(p, α_γ)^{16}O reaction, assuming interference effects between the 11 keV and 323 keV resonances: (a) present results, (b) comparison to the calculations of SP00. The previous experimental data of SP00 are taken from their Table 2 and two curves are digitized from their Figure 6.

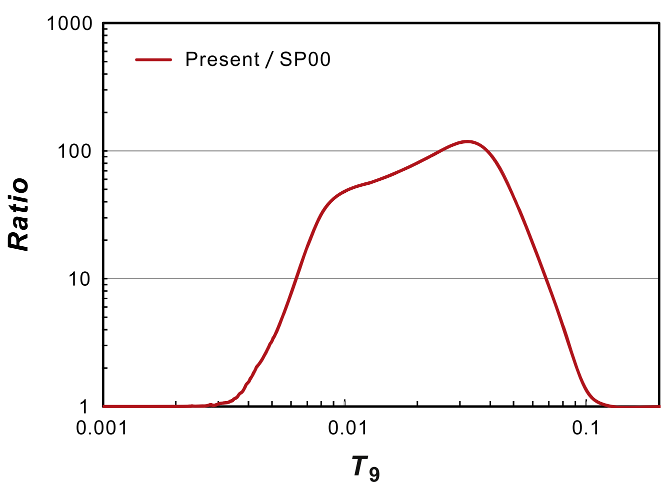

Figure 3. Ratio of the present ^{19}F(p, α_γ)^{16}O rate relative to that of SP00 in temperature region 0.001–0.2 GK. The S factor used in our revised rate calculations is the $\Gamma_{E_r=11} = 1587$ eV curve shown in Figure 2, while SP00 used the $\Gamma_{E_r=11} = 30$ eV curve shown in Figure 2(b).

cross sections (σ) using Equation (8) of SP97, i.e.:

$$\sigma = y/(p_F \times x), \tag{1}$$

with a CaF_2 thickness of $x = 44 \pm 3\ \mu g/cm^2$ and fluorine content of $p_F = 0.38 \pm 0.03$ determined by SP97. We estimate

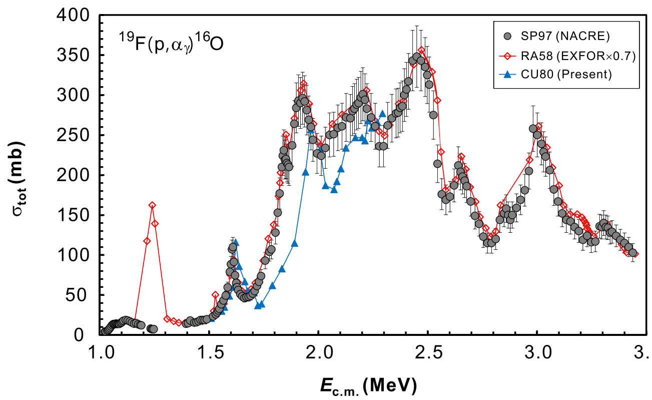

Figure 4. Cross sections of ^{19}F(p, α_γ)^{16}O in Region II. Here, "SP97 (NACRE)" are taken from Table 3 of SP97, as adopted by the NACRE compilation; "RA58 (EXFOR × 0.7)" are originally taken from the EXFOR library and multiplied by a factor of 0.7 to agree with the SP97 data; "CU80 (Present)" are originally taken from the EXFOR library. Here, we corrected the corresponding energy scale by a target thickness of $\Delta = 30$ keV for RA58 and by $\Delta = 3$ keV for CU80, respectively. These target thickness effects are not considered in the ^{19}F(p, α_γ)^{16}O data compiled in the EXFOR library. It should be noted that data for the five narrow resonances in the energy region of 1.0–1.5 MeV were removed from Table 3 of SP97, and are not shown in the "SP97 (NACRE)" data set. Here, the lines connecting the data are just to guide the eyes.

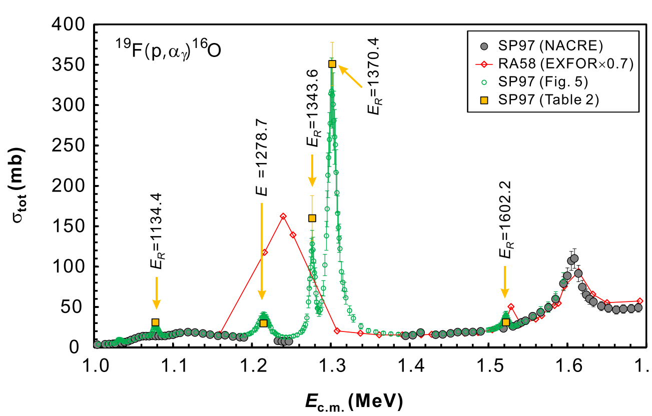

Figure 5. A zoom-in of Figure 4, for the energy range 1.0–1.7 MeV and with additional two data sets of SP97. Where, "SP97 (Figure 5)" indicates the cross sections calculated by Equation (1) based on the yield data shown in Figure 5 of SP97, with an estimated uncertainty of 13%; "SP97 (Table 2)" indicate five data points listed in Table 2 of SP97. The arrows mark the locations of the five resonances listed in Table 2 of SP97, with E_R labeled in the frame. As with Figure 4, these five narrow resonances are not shown in the "SP97 (NACRE)" data set, and the line connecting the RA58 data is just to guide the eyes.

a total uncertainty of 13% for these derived cross sections, i.e., 6.8% for x, 7.9% for p_F, and 7.8% for y (6% for efficiency ϵ, 5% for statistics). There are five resonances indicated by the arrows in Figure 5, i.e., $E_r^{lab} = 1134.4$, 1278.7, 1343.6, 1370.4, and 1602.2 keV, listed in Table 2 of SP97. The corresponding widths are $\Gamma = 2.5$, 16.2, 4.0, 11.9, and 2.7 keV, respectively. The $44 \pm 3\ \mu g\ cm^{-2}$ CaF_2 target thickness is roughly $\Delta = 6.5$ keV in this energy range. Thus, the second and fourth resonances can be regarded as "broad", and their cross-section can be calculated by Equation (1) appropriately. Although Equation (1) does not exactly hold for the remaining three narrow resonances, two data sets labeled as "SP97 (Figure 5)" and "SP97 (Table 2)" in Figure 5, are consistent within the relative large uncertainties for the five resonances shown. It

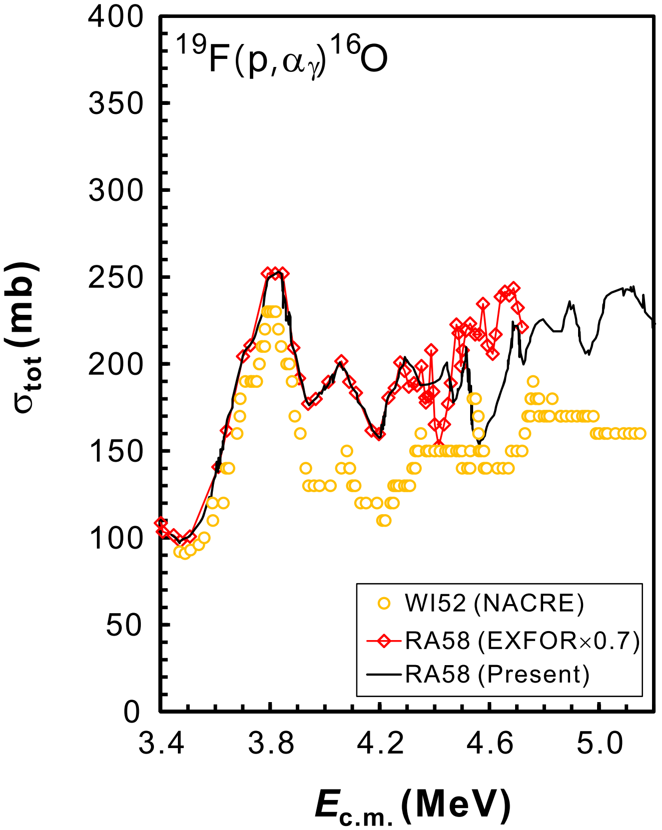

Figure 6. Cross sections of ^{19}F(p, α_γ)^{16}O in Region III. Here, "WI52 (NACRE)" is the same as adopted by NACRE; "RA58 (EXFOR × 0.7)" is the same as in Figure 4 but for the higher energy region (their data digitized above 4.3 MeV are unreliable; see details at footnote 4); "RA58 (Present)" is presently re-digitized from the curve in Figure 1 of RA58 with a multiplying factor of 0.7 for the cross sections by considering a target thickness effect of $\Delta = 30$ keV. The present digitization procedure causes the "RA58 (Present)" curve showing some junk data, which do not affect the rate calculations noticeably. See text for details.

should be noted that for the non-resonant or broad resonance region, the cross sections (based on the yields) agree well with the "SP97 (NACRE)" data, which in fact utilized the same procedure to deduce the cross sections. In addition, the very old RA58 data in the energy region of 1.16–1.34 MeV are probably unreliable. This is because SP97 clearly observed three resonances in this region and these resonances cannot behave as such a broad peak at 1.24 MeV (see Figure 5) as observed by RA58 with a thin target.

We conclude by confirming the S factor (or cross sections) data adopted by NACRE based on SP97. However, the SP97 S factor data (listed in the Table 3 of SP97) excluded the resonant contributions as discussed in the previous subsection, which need to be added to calculate the total (p, α_γ) rate.

2.3. Region III: 3.45 MeV < $E_{c.m.}$ < 5.17 MeV (Figure 6)

In the NACRE compilation, the Willard et al. (1952) data (hereafter, WI52) were adopted for the energy region of $E_{c.m.} > 3.44$ MeV by normalizing to a value of $\sigma = 300$ mb at the $E_{c.m.} = 2.2$ MeV of SP97, with a label "WI52 (NACRE) in the plot. As in Figure 6, the "RA58 (EXFOR × 0.7)" data are shown for the higher energy region. Here, we have re-digitized the curve in Figure 1 of RA58, and normalized the data by a factor of 0.7. Thus, the obtained "RA58 (Present)" data are shown as the black solid curve, which agree very well with the "RA58 (EXFOR × 0.7)" data in the region of 3.4 ∼ 4.3 MeV, beyond which they are quite different. Therefore, we confirmed that the RA58 data compiled in the EXFOR library below 4.3 MeV are correct, but above this energy, their data are unreliable.[10] The WI52 data are generally lower than the RA58 data, especially beyond the 3.9 MeV region, and this reduction might be owing to the carbon deposition as they observed, and also the target material loss as we recently observed (Zhang et al. 2019). We have averaged the "WI52 (NACRE)" and "RA58 (Present)" data in this Region III with an overall conservative uncertainty of 20% assumed (NACRE assumed the uncertainties of WI52 data by 13%–16%).

We have studied the sensitivity of the ^{19}F(p, α_γ)^{16}O rate to the high-energy data in Region III, and found that these high energy data only slightly change the rate above 4 GK, at most about 15% up to 10 GK. Compared to the case without using these high-energy data, the (p, α_γ) rates increase at most by 14%, 15%, and 13% up to 10 GK, using the presently averaged "RA58 (EXFOR×0.7)" and "WI52 (NACRE)" data, respectively. In other words, the high temperature rates are not very sensitive to these high-energy data, simply because of the very broad Gamow peak involved in the integration. Here, a temperature of 10 GK corresponds to a Gamow peak at $E_{c.m.} \approx 2.41$ MeV with a width of $\Delta \approx 3.33$ MeV, and thus the Region III data are located only at the margin of the Gamow window. In any case, the averaged "WI52 (NACRE)" and "RA58 (Present)" data in Region III have been included in the calculations for accuracy and completeness.

2.4. ^{19}F(p, α_γ)^{16}O Rate

It is well-known that the reaction rate of a charged-particle induced reaction can be calculated in terms of the astrophysical S factor, by the following equation (Rolfs & Rodney 1988; Angulo et al. 1999):

$$N_A\langle\sigma v\rangle = N_A\left(\frac{8}{\pi\mu}\right)^{1/2}\frac{1}{(kT)^{3/2}} \int_0^\infty S(E)\exp\left[-\frac{E}{kT} - 2\pi\eta\right]dE. \quad (2)$$

The quantity η is called the Sommerfeld parameter and defined as $\eta = Z_1Z_2e^2/\hbar v$. In numerical units, the exponent is $2\pi\eta = 31.29\, Z_1Z_2\sqrt{\mu/E}$, where the center-of-mass energy E is given in units of keV and the reduced mass μ is in amu. The quantity $\exp(-2\pi\eta)$ is the Coulomb barrier penetration probability and μ is calculated with a proton mass of 1.007276 amu, and ^{19}F mass of 18.993466 amu (Wang et al. 2017). If one simply approximates proton and ^{19}F mass as 1 amu and 19 amu, the calculated penetration factor of exp(-2 $\pi\eta$) will be quite different from the precise one at low energies; in other words, the approximation of mass values can considerably affect the reaction rate calculated for the low-temperature region (He et al. 2018). The cross sections evaluated above can be converted to the astrophysical S factors by the following equation (Rolfs & Rodney 1988;

[10] In fact, the x-axis scale shown in Figure 1 of RA58 is a bit strange, neither linear nor logarithmic; the digitizing procedure in the EXFOR library for RA58 might cause problems due to carelessness.

Table 2
Thermonuclear Reaction Rate of ^{19}F(p, α_γ)^{16}O in Units of cm^{3}s^{-1}mol^{-1} (for the bare ^{19}F Nuclei in the Laboratory, i.e., with no Thermally Excited Target States Considered).

T_9	Median Rate	Low Rate	High Rate	IN17 [a]
0.001	1.72×10^{-74}	$\mathbf{5.42 \times 10^{-86}}$	$\mathbf{1.67 \times 10^{-61}}$	
0.002	2.81×10^{-47}	$\mathbf{2.24 \times 10^{-52}}$	$\mathbf{8.46 \times 10^{-41}}$	
0.003	2.66×10^{-38}	$\mathbf{3.76 \times 10^{-41}}$	$\mathbf{5.36 \times 10^{-34}}$	
0.004	8.67×10^{-34}	$\mathbf{1.54 \times 10^{-35}}$	$\mathbf{1.18 \times 10^{-30}}$	
0.005	6.61×10^{-31}	$\mathbf{3.72 \times 10^{-32}}$	$\mathbf{1.09 \times 10^{-28}}$	
0.010	6.26×10^{-23}	$\mathbf{3.06 \times 10^{-25}}$	$\mathbf{1.44 \times 10^{-22}}$	
0.013	2.99×10^{-20}	$\mathbf{1.99 \times 10^{-22}}$	$\mathbf{6.99 \times 10^{-20}}$	6.22×10^{-22}
0.015	6.96×10^{-19}	$\mathbf{6.24 \times 10^{-21}}$	$\mathbf{1.65 \times 10^{-18}}$	1.77×10^{-20}
0.018	3.07×10^{-17}	$\mathbf{4.14 \times 10^{-19}}$	$\mathbf{7.42 \times 10^{-17}}$	1.00×10^{-18}
0.020	2.45×10^{-16}	$\mathbf{4.21 \times 10^{-18}}$	$\mathbf{6.00 \times 10^{-16}}$	9.68×10^{-18}
0.025	1.54×10^{-14}	$\mathbf{4.26 \times 10^{-16}}$	$\mathbf{3.89 \times 10^{-14}}$	7.71×10^{-16}
0.03	3.51×10^{-13}	$\mathbf{1.39 \times 10^{-14}}$	$\mathbf{9.19 \times 10^{-13}}$	
0.04	3.16×10^{-11}	$\mathbf{2.25 \times 10^{-12}}$	$\mathbf{8.74 \times 10^{-11}}$	2.17×10^{-12}
0.05	7.22×10^{-10}	$\mathbf{8.46 \times 10^{-11}}$	$\mathbf{2.11 \times 10^{-09}}$	1.63×10^{-10}
0.06	7.42×10^{-09}	$\mathbf{1.35 \times 10^{-09}}$	$\mathbf{2.30 \times 10^{-08}}$	
0.07	4.58×10^{-08}	$\mathbf{1.24 \times 10^{-08}}$	$\mathbf{1.49 \times 10^{-07}}$	1.33×10^{-08}
0.08	2.11×10^{-07}	$\mathbf{8.40 \times 10^{-08}}$	$\mathbf{6.83 \times 10^{-07}}$	
0.09	9.54×10^{-07}	$\mathbf{4.95 \times 10^{-07}}$	$\mathbf{2.49 \times 10^{-06}}$	6.16×10^{-07}
0.10	4.46×10^{-06}	$\mathbf{2.89 \times 10^{-06}}$	$\mathbf{8.24 \times 10^{-06}}$	
0.15	3.99×10^{-03}	$\mathbf{3.64 \times 10^{-03}}$	$\mathbf{4.25 \times 10^{-03}}$	
0.20	4.25×10^{-01}	$\mathbf{4.10 \times 10^{-01}}$	$\mathbf{4.36 \times 10^{-01}}$	4.25×10^{-01}
0.25	$1.04 \times 10^{+01}$	$\mathbf{1.02 \times 10^{+01}}$	$\mathbf{1.07 \times 10^{+01}}$	$1.02 \times 10^{+01}$
0.30	$9.19 \times 10^{+01}$	$\mathbf{8.96 \times 10^{+01}}$	$\mathbf{9.41 \times 10^{+01}}$	$7.45 \times 10^{+01}$
0.35	$4.28 \times 10^{+02}$	$\mathbf{4.18 \times 10^{+02}}$	$\mathbf{4.39 \times 10^{+02}}$	$3.66 \times 10^{+02}$
0.40	$1.33 \times 10^{+03}$	$\mathbf{1.30 \times 10^{+03}}$	$\mathbf{1.37 \times 10^{+03}}$	$1.21 \times 10^{+03}$
0.45	$3.18 \times 10^{+03}$	$\mathbf{3.10 \times 10^{+03}}$	$\mathbf{3.26 \times 10^{+03}}$	$3.06 \times 10^{+03}$
0.5	$6.28 \times 10^{+03}$	$\mathbf{6.13 \times 10^{+03}}$	$\mathbf{6.44 \times 10^{+03}}$	$5.94 \times 10^{+03}$
0.6	$1.71 \times 10^{+04}$	$\mathbf{1.67 \times 10^{+04}}$	$\mathbf{1.75 \times 10^{+04}}$	$1.50 \times 10^{+04}$
0.7	$3.46 \times 10^{+04}$	$\mathbf{3.38 \times 10^{+04}}$	$\mathbf{3.55 \times 10^{+04}}$	$3.34 \times 10^{+04}$
0.8	$5.89 \times 10^{+04}$	$\mathbf{5.75 \times 10^{+04}}$	$\mathbf{6.03 \times 10^{+04}}$	$4.98 \times 10^{+04}$
0.9	$9.02 \times 10^{+04}$	$\mathbf{8.81 \times 10^{+04}}$	$\mathbf{9.25 \times 10^{+04}}$	$8.47 \times 10^{+04}$
1.0	$1.29 \times 10^{+05}$	$\mathbf{1.26 \times 10^{+05}}$	$\mathbf{1.33 \times 10^{+05}}$	$1.27 \times 10^{+05}$
1.5	$4.86 \times 10^{+05}$	$\mathbf{4.73 \times 10^{+05}}$	$\mathbf{5.00 \times 10^{+05}}$	
2.0	$1.21 \times 10^{+06}$	$\mathbf{1.17 \times 10^{+06}}$	$\mathbf{1.24 \times 10^{+06}}$	
2.5	$2.41 \times 10^{+06}$	$\mathbf{2.33 \times 10^{+06}}$	$\mathbf{2.50 \times 10^{+06}}$	$2.47 \times 10^{+06}$
3.0	$4.27 \times 10^{+06}$	$\mathbf{4.08 \times 10^{+06}}$	$\mathbf{4.48 \times 10^{+06}}$	$4.83 \times 10^{+06}$
3.5	$6.96 \times 10^{+06}$	$\mathbf{6.55 \times 10^{+06}}$	$\mathbf{7.37 \times 10^{+06}}$	
4.0	$1.05 \times 10^{+07}$	$\mathbf{9.81 \times 10^{+06}}$	$\mathbf{1.12 \times 10^{+07}}$	$1.22 \times 10^{+07}$
5.0	$2.00 \times 10^{+07}$	$\mathbf{1.84 \times 10^{+07}}$	$\mathbf{2.17 \times 10^{+07}}$	$2.08 \times 10^{+07}$
6.0	$3.18 \times 10^{+07}$	$\mathbf{2.90 \times 10^{+07}}$	$\mathbf{3.46 \times 10^{+07}}$	
7.0	$4.45 \times 10^{+07}$	$\mathbf{4.06 \times 10^{+07}}$	$\mathbf{4.86 \times 10^{+07}}$	
8.0	$5.73 \times 10^{+07}$	$\mathbf{5.23 \times 10^{+07}}$	$\mathbf{6.25 \times 10^{+07}}$	
9.0	$6.96 \times 10^{+07}$	$\mathbf{6.35 \times 10^{+07}}$	$\mathbf{7.58 \times 10^{+07}}$	
10.0	$8.09 \times 10^{+07}$	$\mathbf{7.39 \times 10^{+07}}$	$\mathbf{8.80 \times 10^{+07}}$	

Note.
[a] Calculated based on the rates listed in Table 4 of IN17, but neglecting the (p, α_π) contribution.

Angulo et al. 1999):

$$S(E) = \sigma(E) E \exp(2\pi\eta). \tag{3}$$

For the resonant contribution described in Section 2.2.1, the reaction rate can be calculated analytically by the following equation (Schatz et al. 2005; Lam et al. 2016):

$$N_A\langle\sigma v\rangle_{\rm r} = 1.54 \times 10^{11}(\mu T_9)^{-3/2} \times \sum_i \omega\gamma_i \exp\left(-\frac{11.605 E_{\rm r}^i}{T_9}\right) \tag{4}$$

with the resonance parameters listed in Table 1. We have calculated all reaction rates and associated uncertainties based on the Monte Carlo techniques described by Longland et al. (2010). For the narrow resonances listed in Table 1, the probability density function of resonance energies is described by Gaussian distributions, while the resonance strengths (or partial widths) are described by lognormal distributions. For the broad resonance and non-resonant contribution, we adopted the experimental data as discussed in Section 2.2.2 and Section 2.3, and thus the calculated rate uncertainties were dominated by the statistical and systematical errors of Gaussian distributions. Similar to Longland et al. (2010), this procedure results in a "Median rate" which agrees under certain conditions with the commonly reported recommended rate, and a "Low rate" and a "High rate", corresponding to the 0.16 and 0.84 quantiles of the cumulative reaction rate distribution as the uncertainties. The presently calculated ^{19}F(p, α_γ)^{16}O rates and the associated uncertainties (low and high) are listed in Table 2.

3. Total ^{19}F(p, α)^{16}O Rate

The total thermonuclear ^{19}F(p, α)^{16}O rate is the sum of three rates, i.e., for the (p, α_0), (p, α_π), and (p, α_γ) channels. For the (p, α_γ) channel, we have utilized the present results as calculated above. As for the (p, α_0) and (p, α_π) channel, we have recalculated their reaction rates by using the recently evaluated data of He et al. (2018) and Lombardo et al. (2019), respectively, by using the same Monte Carlo techniques as described above. For accuracy, we have included the (p, α_π) contribution in the calculation, although it only plays a very minor role in the total rate.

The present median rate and the associated uncertainties (low and high rates) are listed in Table 3. The present median rate can be parameterized by the standard format of Rauscher & Thielemann (2000) as:

$$\begin{aligned}
N_A\langle\sigma v\rangle = {} & \exp(330.835 - \frac{0.0802857}{T_9} - \frac{38.9613}{T_9^{1/3}} \\
& - 2384.99 T_9^{1/3} + 27061 T_9 \\
& - 154573 T_9^{5/3} - 26.1632 \ln T_9) \\
& + \exp(11.7329 - \frac{0.000139291}{T_9} - \frac{23.1721}{T_9^{1/3}} \\
& - 28.164 T_9^{1/3} + 269.471 T_9 \\
& - 476.158 T_9^{5/3} - 10.4367 \ln T_9) \\
& + \exp(-57.9076 - \frac{3.8551}{T_9} - \frac{50.361}{T_9^{1/3}} \\
& + 131.115 T_9^{1/3} - 7.57744 T_9 \\
& + 0.370116 T_9^{5/3} - 53.7802 \ln T_9) \\
& + \exp(-158.2 - \frac{6.29847}{T_9} + \frac{143.769}{T_9^{1/3}} \\
& + 81.7629 T_9^{1/3} - 61.7046 T_9 \\
& + 8.68783 T_9^{5/3} + 58.1395 \ln T_9),
\end{aligned}$$

with a fitting error of less than 0.7% over the entire temperature region of 0.001–10 GK.

Table 3
Thermonuclear Reaction Rates of ^{19}F(p, α)^{16}O in Units of cm^{3}s^{-1}mol^{-1}

	Present Work			NACRE[a]	CF88 [b]	IN17 [c]
T_9	Median Rate	Low Rate	High Rate			
0.001	4.00×10^{-66}	$\mathbf{1.34 \times 10^{-66}}$	$\mathbf{1.67 \times 10^{-61}}$	5.51×10^{-66}	7.87×10^{-66}	
0.002	2.82×10^{-47}	$\mathbf{7.06 \times 10^{-50}}$	$\mathbf{8.46 \times 10^{-41}}$	5.91×10^{-50}	8.50×10^{-50}	
0.003	2.67×10^{-38}	$\mathbf{4.18 \times 10^{-41}}$	$\mathbf{5.36 \times 10^{-34}}$	3.54×10^{-42}	5.12×10^{-42}	
0.004	8.68×10^{-34}	$\mathbf{1.57 \times 10^{-35}}$	$\mathbf{1.18 \times 10^{-30}}$	2.84×10^{-37}	4.15×10^{-37}	
0.005	6.62×10^{-31}	$\mathbf{3.83 \times 10^{-32}}$	$\mathbf{1.09 \times 10^{-28}}$	8.74×10^{-34}	1.29×10^{-33}	
0.010	6.48×10^{-23}	$\mathbf{2.57 \times 10^{-24}}$	$\mathbf{1.46 \times 10^{-22}}$	1.78×10^{-24}	2.60×10^{-24}	
0.013	3.19×10^{-20}	$\mathbf{2.24 \times 10^{-21}}$	$\mathbf{7.18 \times 10^{-20}}$	1.68×10^{-21}	2.54×10^{-21}	2.87×10^{-21}
0.015	7.61×10^{-19}	$\mathbf{7.25 \times 10^{-20}}$	$\mathbf{1.71 \times 10^{-18}}$	5.52×10^{-20}	8.45×10^{-20}	9.13×10^{-20}
0.018	3.52×10^{-17}	$\mathbf{4.82 \times 10^{-18}}$	$\mathbf{7.86 \times 10^{-17}}$	3.72×10^{-18}	5.78×10^{-18}	5.94×10^{-18}
0.020	2.90×10^{-16}	$\mathbf{4.86 \times 10^{-17}}$	$\mathbf{6.45 \times 10^{-16}}$	3.76×10^{-17}	5.92×10^{-17}	5.97×10^{-17}
0.025	2.02×10^{-14}	$\mathbf{5.02 \times 10^{-15}}$	$\mathbf{4.37 \times 10^{-14}}$	3.88×10^{-15}	6.26×10^{-15}	5.94×10^{-15}
0.03	5.18×10^{-13}	$\mathbf{1.72 \times 10^{-13}}$	$\mathbf{1.09 \times 10^{-12}}$	1.33×10^{-13}	2.19×10^{-13}	
0.04	6.15×10^{-11}	$\mathbf{3.02 \times 10^{-11}}$	$\mathbf{1.18 \times 10^{-10}}$	2.27×10^{-11}	3.91×10^{-11}	3.34×10^{-11}
0.05	1.97×10^{-09}	$\mathbf{1.21 \times 10^{-09}}$	$\mathbf{3.37 \times 10^{-09}}$	8.72×10^{-10}	1.56×10^{-09}	1.43×10^{-09}
0.06	2.97×10^{-08}	$\mathbf{2.04 \times 10^{-08}}$	$\mathbf{4.45 \times 10^{-08}}$	1.41×10^{-08}	2.61×10^{-08}	
0.07	2.66×10^{-07}	$\mathbf{1.94 \times 10^{-07}}$	$\mathbf{3.55 \times 10^{-07}}$	1.30×10^{-07}	2.48×10^{-07}	2.22×10^{-07}
0.08	1.62×10^{-06}	$\mathbf{1.22 \times 10^{-06}}$	$\mathbf{2.01 \times 10^{-06}}$	8.13×10^{-07}	1.59×10^{-06}	
0.09	7.42×10^{-06}	$\mathbf{5.74 \times 10^{-06}}$	$\mathbf{8.86 \times 10^{-06}}$	3.95×10^{-06}	7.67×10^{-06}	6.76×10^{-06}
0.10	2.80×10^{-05}	$\mathbf{2.23 \times 10^{-05}}$	$\mathbf{3.26 \times 10^{-05}}$	1.65×10^{-05}	2.98×10^{-05}	
0.15	6.29×10^{-03}	$\mathbf{5.78 \times 10^{-03}}$	$\mathbf{6.64 \times 10^{-03}}$	6.92×10^{-03}	4.47×10^{-03}	
0.20	4.71×10^{-01}	$\mathbf{4.54 \times 10^{-01}}$	$\mathbf{4.84 \times 10^{-01}}$	5.12×10^{-01}	3.67×10^{-01}	4.60×10^{-01}
0.25	$1.08 \times 10^{+01}$	$\mathbf{1.05 \times 10^{+01}}$	$\mathbf{1.11 \times 10^{+01}}$	$1.09 \times 10^{+01}$	$9.57 \times 10^{+00}$	$1.05 \times 10^{+01}$
0.30	$9.38 \times 10^{+01}$	$\mathbf{9.15 \times 10^{+01}}$	$\mathbf{9.61 \times 10^{+01}}$	$9.26 \times 10^{+01}$	$8.66 \times 10^{+01}$	$7.59 \times 10^{+01}$
0.35	$4.35 \times 10^{+02}$	$\mathbf{4.24 \times 10^{+02}}$	$\mathbf{4.46 \times 10^{+02}}$	$4.26 \times 10^{+02}$	$4.15 \times 10^{+02}$	$3.71 \times 10^{+02}$
0.40	$1.35 \times 10^{+03}$	$\mathbf{1.32 \times 10^{+03}}$	$\mathbf{1.38 \times 10^{+03}}$	$1.32 \times 10^{+03}$	$1.35 \times 10^{+03}$	$1.22 \times 10^{+03}$
0.45	$3.22 \times 10^{+03}$	$\mathbf{3.14 \times 10^{+03}}$	$\mathbf{3.30 \times 10^{+03}}$	$3.14 \times 10^{+03}$	$3.48 \times 10^{+03}$	$3.09 \times 10^{+03}$
0.5	$6.36 \times 10^{+03}$	$\mathbf{6.21 \times 10^{+03}}$	$\mathbf{6.52 \times 10^{+03}}$	$6.21 \times 10^{+03}$	$7.72 \times 10^{+03}$	$5.99 \times 10^{+03}$
0.6	$1.74 \times 10^{+04}$	$\mathbf{1.70 \times 10^{+04}}$	$\mathbf{1.78 \times 10^{+04}}$	$1.70 \times 10^{+04}$	$2.93 \times 10^{+04}$	$1.52 \times 10^{+04}$
0.7	$3.53 \times 10^{+04}$	$\mathbf{3.44 \times 10^{+04}}$	$\mathbf{3.61 \times 10^{+04}}$	$3.47 \times 10^{+04}$	$8.77 \times 10^{+04}$	$3.39 \times 10^{+04}$
0.8	$6.03 \times 10^{+04}$	$\mathbf{5.89 \times 10^{+04}}$	$\mathbf{6.17 \times 10^{+04}}$	$5.96 \times 10^{+04}$	$2.16 \times 10^{+05}$	$5.09 \times 10^{+04}$
0.9	$9.29 \times 10^{+04}$	$\mathbf{9.07 \times 10^{+04}}$	$\mathbf{9.51 \times 10^{+04}}$	$9.25 \times 10^{+04}$	$4.55 \times 10^{+05}$	$8.68 \times 10^{+04}$
1.0	$1.34 \times 10^{+05}$	$\mathbf{1.31 \times 10^{+05}}$	$\mathbf{1.37 \times 10^{+05}}$	$1.35 \times 10^{+05}$	$8.42 \times 10^{+05}$	$1.31 \times 10^{+05}$
1.5	$5.26 \times 10^{+05}$	$\mathbf{5.12 \times 10^{+05}}$	$\mathbf{5.39 \times 10^{+05}}$	$5.48 \times 10^{+05}$	$5.73 \times 10^{+06}$	
2.0	$1.37 \times 10^{+06}$	$\mathbf{1.34 \times 10^{+06}}$	$\mathbf{1.41 \times 10^{+06}}$	$1.47 \times 10^{+06}$	$1.53 \times 10^{+07}$	
2.5	$2.88 \times 10^{+06}$	$\mathbf{2.80 \times 10^{+06}}$	$\mathbf{2.97 \times 10^{+06}}$	$3.13 \times 10^{+06}$	$2.78 \times 10^{+07}$	$2.87 \times 10^{+06}$
3.0	$5.29 \times 10^{+06}$	$\mathbf{5.10 \times 10^{+06}}$	$\mathbf{5.49 \times 10^{+06}}$	$5.77 \times 10^{+06}$	$4.15 \times 10^{+07}$	$5.68 \times 10^{+06}$
3.5	$8.76 \times 10^{+06}$	$\mathbf{8.36 \times 10^{+06}}$	$\mathbf{9.18 \times 10^{+06}}$	$9.53 \times 10^{+07}$	$5.52 \times 10^{+07}$	
4.0	$1.33 \times 10^{+07}$	$\mathbf{1.26 \times 10^{+07}}$	$\mathbf{1.40 \times 10^{+07}}$	$1.44 \times 10^{+07}$	$6.84 \times 10^{+07}$	$1.45 \times 10^{+07}$
5.0	$2.52 \times 10^{+07}$	$\mathbf{2.36 \times 10^{+07}}$	$\mathbf{2.68 \times 10^{+07}}$	$2.70 \times 10^{+07}$	$9.23 \times 10^{+07}$	$2.49 \times 10^{+07}$
6.0	$3.94 \times 10^{+07}$	$\mathbf{3.66 \times 10^{+07}}$	$\mathbf{4.22 \times 10^{+07}}$	$4.19 \times 10^{+07}$	$1.13 \times 10^{+08}$	
7.0	$5.44 \times 10^{+07}$	$\mathbf{5.05 \times 10^{+07}}$	$\mathbf{5.84 \times 10^{+07}}$	$5.76 \times 10^{+07}$	$1.30 \times 10^{+08}$	
8.0	$6.92 \times 10^{+07}$	$\mathbf{6.42 \times 10^{+07}}$	$\mathbf{7.44 \times 10^{+07}}$	$7.30 \times 10^{+07}$	$1.45 \times 10^{+08}$	
9.0	$8.31 \times 10^{+07}$	$\mathbf{7.71 \times 10^{+07}}$	$\mathbf{8.94 \times 10^{+07}}$	$8.74 \times 10^{+07}$	$1.57 \times 10^{+08}$	
10.0	$9.58 \times 10^{+07}$	$\mathbf{8.89 \times 10^{+07}}$	$\mathbf{1.03 \times 10^{+08}}$	$1.00 \times 10^{+08}$	$1.68 \times 10^{+08}$	

Notes. Here, all listed rates are for the bare ^{19}F nuclei in the laboratory, i.e., no thermally excited target states are considered.
[a] Rates adopted from NACRE;
[b] Rates calculated by the analytical equation of CF88;
[c] Rates adopted from Table 4 of IN17.

The ratios relative to the NACRE recommended ^{19}F(p, α)^{16}O rate are shown in Figure 7 for the present total rate, and the rates of Caughlan & Fowler (1988; hereafter, CF88) and of Indelicato et al. (2017; hereafter, IN17). The uncertainties for the present and NACRE rates are shown as the error bands. The present rate agrees well with the NACRE rate above 0.25 GK, however, at lower temperature, it is remarkably larger than the previous rates. For instance, the present rate is larger than NACRE by factors of 36.4, 2.3, and 1.7 at temperatures of 0.01, 0.05, and 0.1 GK, respectively; and it is about four orders of magnitude larger around 0.003 GK, although the reaction maybe not activated at such a low temperature. The significant deviations are caused by the fact that the present extrapolated low-energy (p, α_γ) S factor (as shown in Figure 2) are much larger than those recommended by SP00 with $\Gamma_{E_r=11} = 30$ eV, and that the NACRE rate did not consider the interference effect at all. These enhanced low-energy S factor owing to the interference effect result in a much larger (p, α_γ) rate and hence a larger total (p, α) rate. The very large uncertainty for the present rate below 0.1 GK is mainly to be attributed to those in the (p, α_0) and (p, α_γ) rates, while below $\sim$0.02 GK, it is overwhelmingly dominated by the energy uncertainty

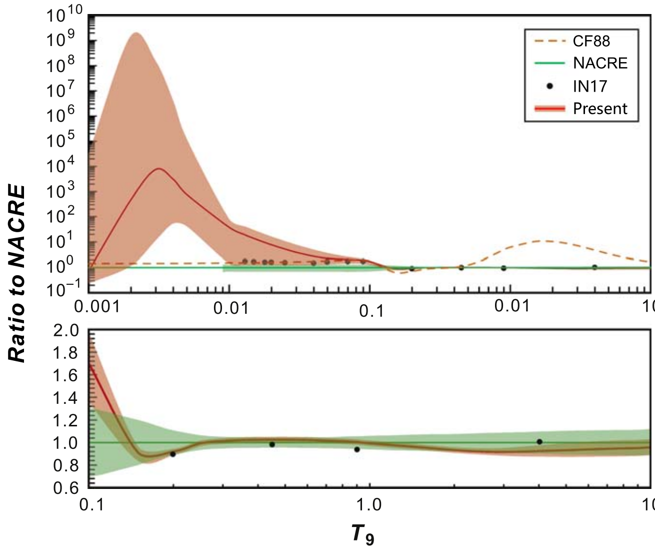

Figure 7. The reaction rate ratios relative to the NACRE recommended ^{19}F(p, α)^{16}O rate. The CF88, NACRE, and IN17 rates are from Caughlan & Fowler (1988), Angulo et al. (1999), and Indelicato et al. (2017), respectively. No uncertainties were reported by CF88 and IN17 and by NACRE below 0.009 GK. The lower panel is a zoom of the 0.1–10 T_9 range.

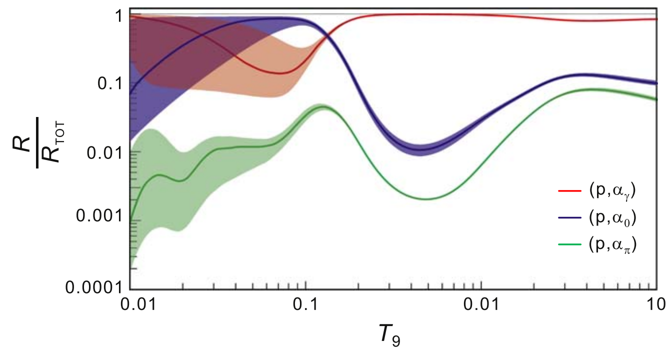

Figure 8. Contribution of each channel to the total reaction rate ($R_{\rm TOT}$). The black dotted line corresponds to $R/R_{\rm TOT} = 1$ as a reference. The respective uncertainties are shown for each channel.

($\pm$2.6 keV) estimated for the lowest resonance at 11 keV (Kious 1990). Therefore, it is very important to precisely determine the location of this resonance, to constrain the low-temperature rate more strictly. Finally, the present rate agrees well with NACRE below 0.003 GK, because both were calculated with the same parameters for the lowest 11 keV resonance. In addition, the recent IN17 rate is a factor of $\sim$1.5–1.7 larger than the NACRE rate below 0.09 GK, because enhanced astrophysical S factor for the (p, α_0) channel were obtained by the Trojan horse method. But the IN17 rate agrees very well with the CF88 rate in the temperature region of 0.01–0.4 GK. It shows that the CF88 rate is the largest above $\sim$0.5 GK, mainly because the contributions from the high-lying resonances were overestimated based on the scarce experimental data at that time.

To show the relative contribution of the three channels, their ratios to the total reaction rate are shown in Figure 8. The (p, α_γ) channel dominates the total rate over the entire temperature region, except in a narrow temperature region of 0.05–0.12 GK where the (p, α_0) channel dominates. The role of the (p, α_0) and (p, α_γ) channels is very different from that shown by IN17, who determined that the (p, α_0) channel dominated at very low temperatures and the (p, α_γ) channel became dominant above 0.2 GK. Low-energy data below 0.2 MeV for both channels are strongly required to constrain the total rate below $\sim$0.2 GK.

The excited levels of a target nucleus can be thermally populated and thus contribute to the reaction mechanism in the stellar plasma environment. Therefore, the presently listed rates for the bare ^{19}F nuclei should be corrected by the stellar enhancement factor (SEF). The nucleus ^{19}F has two very low-lying excited states with $E_x = 0.110$ and 0.198 MeV, and such low excited states can be heavily populated at high temperatures ($T_9 \leqslant 1$) of astrophysical interest. The SEF factor predicted in NACRE (i.e., $1 + 0.755 \times \exp(-1.755/T_9 - 0.174 \times T_9)$) based on the statistical model, is not very large (no more than 25%), as shown in Figure 9. Bahcall & Fowler (1969) made an estimate based on the experimental information of the elastic and inelastic scattering of p+^{19}F, as well as of the (p, α) data. The inclusion of these two excited states of ^{19}F could significantly increase the calculated ^{19}F(p, α)^{16}O rate at temperatures above $\sim$0.7 GK. Here, we draw their SEF data and our extended calculation curve in Figure 9 as a black solid line. This large SEF is mainly caused by three resonance states (at $E_x = 0.598$, 0.710, 1.250 MeV cited by Bahcall & Fowler, 1969) decaying to the two low-lying state in ^{19}F, by very large widths of both Γ_p^1 and Γ_p^2. Since there were no experimental available widths of Γ_p^1 and Γ_p^2 for $E_x = 0.598$ and 0.710 MeV states, Bahcall & Fowler (1969) took the experimental upper limits for the partial widths in order to estimate the maximum possible contributions from the corresponding resonances. Therefore, the SEF estimated by Bahcall & Fowler (1969) is an upper limit. In any case, the SEF discussed above only needs to be considered above $\sim$1 GK; otherwise the bare rate listed in our Table 3 is sufficient for the present stellar model calculations.

4. Astrophysical Implications

The fact that the element fluorine (i.e., monoisotopic ^{19}F) is the least abundant in the solar system among the common light elements from carbon to silicon, is a reflection of the fragile nature of its nucleus in nucleosynthetic environments, including the effect of its proton capture rate investigated here. As mentioned in the 1, its origin in the Galaxy is still a debated topic; see, e.g., recent papers by Grisoni et al. (2020); Ryde et al. (2020), with asymptotic giant branch (AGB) stars and massive Wolf–Rayet star winds as the main contributors, together with winds from fast-rotating massive stars in the early life of the Galaxy. The main production mechanism of ^{19}F in all these environments is connected to He burning, where fluorine is produced directly via the ^{18}O(p, α)^{15}N(α, γ)^{19}F reaction chain. The required ^{18}O nuclei are produced by double α-captures on the abundant ^{14}N, the typical main product of the CNO cycle in the H-burning ashes, and the protons are produced by the ^{14}N(n, p)^{14}C reaction, with neutrons from ^{13}C(α, n)^{16}O, and ^{13}C also from the CNO H-burning ashes (see more details in, e.g., Lugaro et al. 2004). In this context, the ^{19}F(p, α)^{16}O reaction is not relevant because it cannot compete with the ^{18}O(p, α)^{15}N reaction given that the ^{19}F abundance is orders of magnitudes lower than that of ^{18}O.

The ^{19}F(p,α)^{16}O is relevant instead in the context of the CNO cycles of H burning. Because this reaction is much more efficient at low temperatures than the ^{18}O(p,γ)^{19}F reaction; the typical result of H burning is the destruction of ^{19}F, and the

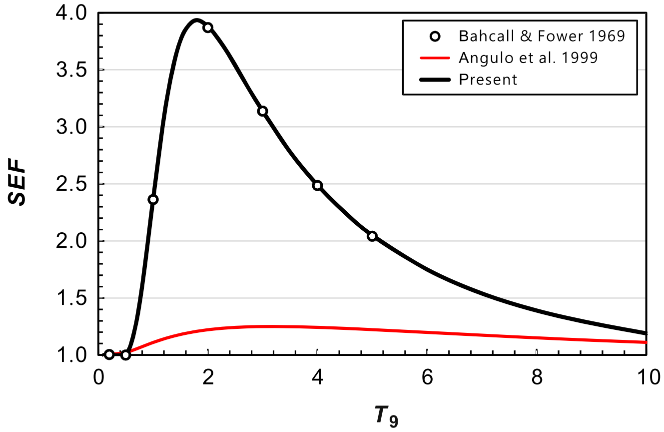

Figure 9. The stellar enhancement factor (SEF) for the $^{19}F(p, \alpha)^{16}O$ reaction. Bahcall & Fowler (1969) listed only seven temperature points ranging from 0.2 GK to 5 GK, and here we extended the calculation in exactly the same way for more temperature points shown as a thick solid line. The factor adopted by NACRE, which was calculated by Angulo et al. (1999) based on the statistical model, is also shown for comparison.

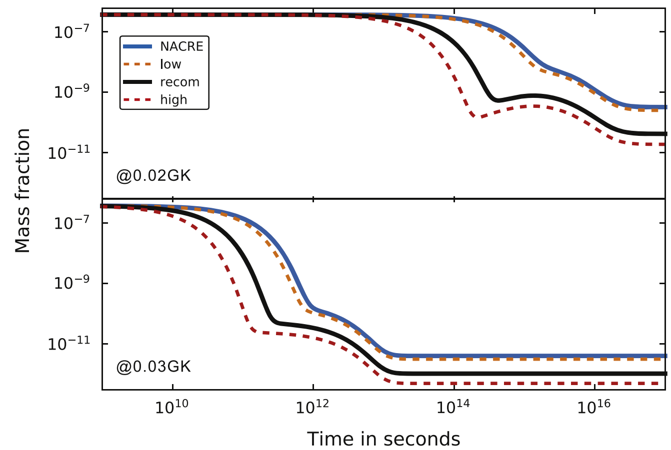

Figure 10. Evolution of ^{19}F in a one-zone simulation of the CNO cycle for different $^{19}F(p,\alpha)^{16}O$ rates and temperatures. The top panel is the simulation result for a temperature of 0.02 GK, and the bottom panel for a temperature of 0.03 GK. In both cases, a density of 100 g/cm^3 was utilized. Here, the labels of recom, low, and high, indicate the present recommended (median) rate and the low and high rate limits (listed in Table 3), respectively.

level of that destruction is controlled by the $^{19}F(p,\alpha)^{16}O$ reaction. We performed a network calculation to simulate the CNO cycle with 57 nuclei, initial solar abundances from Asplund et al. (2009), and the starlib reaction library, version 6[11]. We then modified the $^{19}F(p,\alpha)^{16}O$ reaction rate to the values presented in this work and ran the models with a density of 100 g/cm^3 and temperature 0.02 GK and 0.03 GK (as in Figure 4 of Wiescher et al. 1999). The evolution of the mass fraction of ^{19}F is shown in Figure 10. The time at which ^{19}F starts to be depleted and the final values after the hydrogen is exhausted change significantly depending on the reaction rate considered. While the lower limit of the present rate gives results similar to the NACRE rate, the recommended and the upper limits decrease the final value of ^{19}F by up to one order of magnitude.

We analyze the impact of this change within the specific astrophysical scenario where H burning at relatively low temperature occurs at or below the base of the convective H-rich envelope of AGB stars. In relatively massive AGB stars (with an initial mass higher than roughly 3 $M_\odot$, depending on the metallicity), the base of the envelope is hot enough (with temperatures above 0.06 GK) that H burning occurs directly there in a process usually referred to as "hot bottom burning" and the whole envelope composition is quickly changed into the typical abundances of the CNO cycle. In this case, ^{19}F is always completely destroyed and the net stellar yield is negative (see, e.g., Lugaro et al. 2004; Karakas 2010), reflecting an overall destruction compared to production over the stellar lifetime.

A different picture may arise when considering extra mixing processes at lower temperatures (below 0.06 GK) have been proposed to occur in low-mass AGB stars (initial masses lower than roughly 3 $M_\odot$). In this case, material from the base of the convective envelope slowly circulates into the underlying, hotter radiative layers. This process has been mostly invoked to explain ^{18}O depletion in a specific fraction of meteoritic oxide stardust grains believed to have originated in O-rich AGB stars (Palmerini et al. 2017), although a new rate of the $^{17}O(p, \alpha)^{14}N$

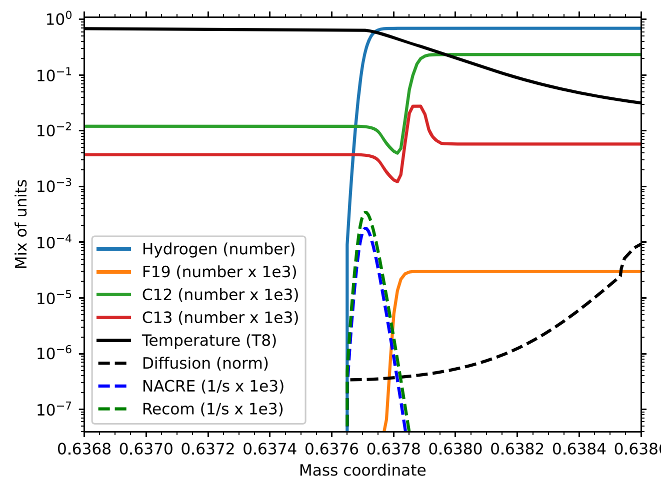

Figure 11. Abundances, temperature, and $^{19}F(p,\alpha)^{16}$ reaction rates from both NACRE and the present recommended rate, and diffusion coefficient profiles for the $O_v = 7$ case as a function of mass around the location of the H-burning shell, at the border between the H-rich envelope (to the right) and the He-rich intershell (to the left, represented by the H-burning ashes) at the time when we start the extra mixing simulations, i.e., corresponding to roughly the middle of the interpulse period, taken as typical. The temperature is in units of 10^8 K, the diffusion coefficient is normalized to its maximum value (of 3.7×10^{-9} $M_\odot$/s), and all the rates and isotopic abundances are multiplied by 10^3, except for hydrogen.

reaction favors an origin in massive AGB stars with "hot bottom burning" for these grains (Lugaro et al. 2017). In any case, if extra mixing occurs in low-mass AGB stars, it may destroy the fluorine produced during the recurrent He-burning thermal pulses and carried into the envelope by the "dredge-up" episodes that may follow these thermal pulses. Such production and mixing of fluorine in AGB stars is demonstrated by observational constraints showing excess F abundances (Abia et al. 2015).

Palmerini et al. (2019) analyzed the possible effect of such extra mixing within an AGB star of initial mass 2 $M_\odot$ and solar metallicity, and the impact of different rates of the $^{19}F(p, \alpha)^{16}O$ reaction on such an effect. They found that the surface

[11] http://starlib.physics.unc.edu/index.html

Table 4
Surface Abundances (in Number Fraction, and with the, e.g., 2.03e-4 Notation Representing 2.03×10^{-4}) of ^{19}F as Derived by Our Model Using Different Rates of the ^{19}F(p, α)^{16}O Reaction

O_v	$M_{\rm env}$ ($M_\odot$)	^{19}F				^{12}C	^{13}C	^{12}C/^{13}C
		NACRE	High	Recommended	Low			
	Solar Value	1.97e-8				2.19e-4	2.45e-6	89
1[a]	0.25–1.3	2.98e-8	2.98e-8	2.98e-8	2.98e-8	2.33e-4	5.78e-6	40.34
3	0.25	2.45e-8	**2.40e-8**	**2.42e-8**	**2.44e-8**	1.83e-4	6.12e-6	29.84
	0.5	2.67e-8	**2.64e-8**	2.65e-8	2.66e-8	2.03e-4	6.04e-6	33.67
	1.3	2.85e-8	2.84e-8	2.84e-8	2.84e-8	2.21e-4	5.91e-6	37.38
4	0.25	5.25e-9	**4.64e-9**	**4.88e-9**	**5.10e-9**	3.04e-5	2.41e-6	12.63
	0.5	1.14e-8	**1.06e-8**	1.09e-8	**1.12e-8**	7.53e-5	4.24e-6	17.78
	1.3	2.02e-8	**1.97e-8**	1.99e-8	**2.01e-8**	1.48e-4	5.61e-6	26.45
5	0.25	5.08e-11	**3.46e-11**	**4.02e-11**	**4.58e-11**	1.67e-7	2.74e-8	6.09
	0.5	8.63e-10	**6.99e-10**	**7.58e-10**	**8.16e-10**	4.18e-6	4.69e-7	8.92
	1.3	7.21e-9	**6.61e-9**	6.84e-9	**7.03e-9**	4.65e-5	2.95e-6	15.78
7	0.25	4.45e-20	**9.75e-21**	**1.68e-20**	**2.74e-20**	1.82e-17	5.41e-18	3.36
	0.5	7.84e-15	**3.32-15**	**4.54e-15**	**5.97e-15**	1.18e-11	2.82e-12	4.20
	1.3	6.53e-11	**4.67e-11**	**5.26e-11**	**5.86e-11**	2.63e-7	3.70e-8	7.12
10[b]	1.3	8.95e-16	**2.69e-16**	**3.82e-16**	**5.57e-16**	9.67e-13	2.29e-13	4.22

Notes. The C isotopic abundances are also reported, which are indicative of the efficiency of the mixing process. The initial abundances for all cases are the same as those reported for $O_v = 1$..
[a] The values are identical to the initial values and the same for all $M_{\rm env}$ cases;
[b] In the $M_{\rm env} = 0.25$ and $0.5 M_\odot$ cases, all the abundances are close to zero.

abundance of ^{19}F may change by 50% when changing the rate of this reaction. Here, we reanalyze this impact considering the new thermonuclear ^{19}F(p, α)^{16}O rate rates presented in this work.

We simulate extra mixing during a typical interpulse period using constant temperature, density, convective velocity, and abundance profiles (see Figure 11) extracted from the middle of the interpulse period following the fifth thermal pulse and dredge-up in a $2 M_\odot$ stellar model at solar (Z=0.014) metallicity from Karakas (2014). The abundance difference between the solar values and the initial values used in the simulations (Lines 1 and 2 of Table 4) is due to the operation of the dredge-up, which at the point in time of this particular model resulted in the increase of fluorine and ^{12}C and a decrease of ^{13}C. The maximum temperature reached in the H-rich region is 0.064 GK. The extra mixing below the base of the convective envelope is simulated via diffusion. In the convective envelope we mix according to the classical Mixing Length Theory (MLT) diffusion coefficient (e.g., Herwig et al. 1997). We extend the MLT coefficient inward in mass into the extra mixing region by multiplying it by the exponential term $\exp[-30/O_v \times (r_c - r)/(r_c - r_h)]$, where O_v is the overshoot parameter (which we varied from 1 to 10), r_c is the lower radius of the convective region, r_h is the lower radius of the hydrogen shell, and $r_h \leqslant r \leqslant r_c$. The overshoot coefficient is not extended below r_h following Nollett et al. (2003). We run the simulation for a typical interpulse length of 50,000 yr. Also following Table 1 of Nollett et al. (2003), we present the results with three different envelope masses: 1.3, 0.5, and 0.25 $M_\odot$, to simulate the decreasing envelope mass as a result of strong mass loss via stellar winds. In addition to the ^{19}F(p, α)^{16}O reaction, we also follow two other proton-capture reactions: ^{12}C(p, γ)^{13}N, with the following β-decay of ^{13}N into ^{13}C, considered instantaneous here, and ^{13}C(p, γ)^{14}N. We solve the diffusion-reaction system of equations using operator-splitting with a relative accuracy of 10^{-3}.

In Figure 11 we show the profiles in mass of the initial abundances, temperature, ^{19}F(p, α)^{16} reaction rates, and diffusion coefficient for the $O_v = 7$ case. All these profiles are set by the choice of the initial model and the specific choice does not have a significant effect on the final surface abundances, as long as it is typical. The changes in the abundances at the stellar surface are mostly wrought by the extra mixing assumed to carry the material from the deep layers represented in the figure into the convective envelope, which is mostly controlled by the diffusion coefficient and the ^{19}F(p, α)^{16}O reaction rate. In general, when moving deeper into the star, the abundances of the C isotopes are modified at a mass location close to where the F abundance is also modified, which explains why any significant effect of extra mixing on the abundance of fluorine is necessarily accompanied by a significant effect on the C isotopic abundances and vice versa (see Table 4). Therefore, if AGB stars in the mass range that could have experienced dredge-up are assumed to also experience extra mixing, lowering their C isotopic ratios, these stars should also be somewhat poorer in fluorine, relatively to their counterparts that did not experience extra mixing.

The results from all the models are reported in Table 4. It is possible to obtain a significant operation of extra mixing in our diffusive framework only for O_v parameters larger than 3. Also, by decreasing the mass of the envelope, the effect of extra mixing becomes larger as the material exposed to the burning region is diluted within a smaller mass of initial composition. For $O_v = 4$ to 10, the significant effect of extra mixing is shown by the ^{12}C/^{13}C ratios in Table 4, which becomes lower by a factor from roughly 2 to 10.[12] As expected, the ^{19}F abundance is only affected if the extra mixing is efficient, i.e., if O_v is at

[12] The initial abundance of ^{16}O is unchanged from the adopted initial solar abundance of roughly 4×10^{-4} and the particular model we show here is not C-rich. In any case, when extra mixing is significantly activated it is hardly expected for the envelope to become C-rich, as according to our models, the C abundance decreases by a factor of up to 50.

least as large as 4. In this case, the abundance of ^{19}F decreases by factors of 1.5 to 6, depending on $M_{\rm env}$; modifying the ^{19}F(p, α)^{16}O reaction rate from NACRE to the present values has an impact of at most $\sim$10% because the destruction of F is only partial. For higher values of O_v, the F abundances decreases by several orders of magnitudes. For example, in the $O_v = 7$ case shown in Figure 11, regions in mass with different diffusion coefficients significantly overlap with regions in mass with a significant value of the ^{19}F(p, α)^{16} reaction rate, therefore, the variation in the F surface abundance is more significant. In the relevant temperature range, the rate presented here is roughly a factor of two to three larger than NACRE; therefore, the changes in the F surface abundances between the NACRE rate and the present rate are up to a factor of two to three. However, the largest modification occurs only for cases where the F abundance is already so low that, relatively, they do not have a strong impact in the final results.

5. Summary and Outlook

We have re-evaluated the available astrophysical S factor and cross-section data of the ^{19}F(p, α_γ)^{16}O reaction in the energy region of $E_{\rm c.m.} = 0 \sim 5.2$ MeV and calculated a total thermonuclear ^{19}F(p, α)^{16}O rate in the temperature region of 0.001–10 GK based on the present and previous evaluations. The main result is that in the low temperature region of 0.01–0.1 GK, the present total rate is remarkably larger, by up to a factor of 36.4 around 0.01 GK, than the NACRE recommended rate and the most recent results of Indelicato et al. (2017). This is because we have considered an enhanced low-energy (p, α_γ) S factor, owing to the interference effect between a probable low-energy 11 keV resonance and the well-known 323 keV resonance, and found that the previous low-energy extrapolation is possibly unreliable. Therefore, the existence of the low-energy 11 keV resonance and its properties need more experimental studies via indirect techniques.

The strong increase of our rate at low temperature shows a significant impact on the fluorine destruction in the CNO cycle (see Figure 10), and this general behavior needs to be analyzed further. Here, we have investigated the impact of the new rate on the specific case of extra mixing in AGB stars by considering a simple model within a 2 $M_\odot$ AGB star of solar metallicity. Using the new rates only mildly changes the overall results, a finding that allows us to confirm that AGB stars that suffer extra mixing leading to low ^{12}C/^{13}C ratios and should also present depleted F abundances, relative to AGB stars that do not experience such a phenomenon. This implication is particularly relevant and further investigated at low metallicity in relation to the F abundances observed in carbon-enhanced metal-poor stars (Lucatello et al. 2011). Furthermore, our preliminary calculations are based on a simple parametric model of extra mixing in AGB stars and need to be verified by models based on actual physical mechanisms to drive the extra mixing, such as magnetic fields (Busso et al. 2007; Nucci & Busso 2014; Palmerini et al. 2017).

The China Jinping Underground Nuclear Astrophysics laboratory (JUNA) project (Liu et al. 2016) aims at direct cross-section measurements of key stellar nuclear reactions down to the Gamow windows. Directly measuring the key ^{19}F(p, α)^{16}O reaction at effective burning energies (i.e., at a Gamow window of $E_{\rm c.m.} = 70$–350 keV) with a better accuracy (statistical error of $\sim$10% as a goal) represents one of the scientific research sub-projects (He et al. 2016). Ultimately, direct experimental data will help us to expound on the origin of fluorine in the Galaxy by putting the astrophysical models on a much firmer experimental ground.

The authors are very grateful to the anonymous referee who provided us with an important part of the Kious (1990) Ph.D. thesis as well as valuable comments and suggestions. This work was financially supported by the National Natural Science Foundation of China (No. 11490562, 11825504, 12075027, 11961141004) and the National Key Research and Development Program of China (2016YFA0400503). M.L. gratefully acknowledges financial support from the Lendület grant (LP17-2014) of the Hungarian Academy of Sciences. AIK acknowledges funding from the Australian Government through the Australian Research Council's Discovery Projects funding scheme (project DP170100521) and from the Australian Research Council Centre of Excellence for All Sky Astrophysics in 3 Dimensions (ASTRO 3D) through project number CE170100013.

Appendix A
Re-evaluation of the S factor Presented in Figure 6 of SP00

Using a similar analysis and fit method as described by SP00, we have reanalyzed the low-energy S factor data presented in their Figure 6 including the interference effect between the 11 keV and 323 keV resonances. To perform the fit we need to determine the $\ell_{\rm p}$ values for calculating the proton width[13] in each resonance. Each $\ell_{\rm p}$ value is constrained by the angular momentum conservation law, i.e., the angular momentum of the resonant state (determined by its spin) must be equal to that of the incident channel, $p + {}^{19}$F. Both the proton and the ^{19}F in the ground state have $J^\pi = 1/2^+$, and hence the channel spin can only be $s = 1$ or 0. For instance, for the 323 keV resonance, the corresponding excited state in ^{20}Ne has $J^\pi = 1^+$, and thus $\ell_{\rm p}$ values should be 0 or 2. Other values are forbidden by also considering the parity conservation law. The allowed $\ell_{\rm p}$ values for the seven resonances, which were listed in Table 1 of SP00, are summarized in Table 5. We have tried all the allowed $\ell_{\rm p}$ values for the seven resonances listed in Table 1 of SP00, but none of the allowed combinations well reproduce the two curves in Figure 6 of SP00, i.e., with $\Gamma_{E_{\rm r}=11} = 30$ eV, and 1 keV for the 11 keV resonance. The shape of the curves are sensitive to the ℓ values, which were not given by SP00, and some forbidden $\ell_{\rm p}$ values might have been utilized in their work. We have tried both the allowed and forbidden $\ell_{\rm p}$ values, and found that the SP00's two curves can be reproduced by some specific $\ell_{\rm p}$ combinations for the seven resonances involved. To reproduce the $\Gamma_{E_{\rm r}=11} = 30$ eV curve, the $\ell_{\rm p}$ value for the 323 keV resonance must be 3, while the allowed values are 0 and 2 as discussed above. At the same time, the $\ell_{\rm p}$ value for the 564 keV resonance must be the allowed value of 3. Similarly, to reproduce the $\Gamma_{E_{\rm r}=11} = 1$ keV curve, the $\ell_{\rm p}$ values for both the 323 keV and 564 keV resonances must be 4, which are all forbidden. The comparison between the present results and those of SP00 is shown in Figure 12, where the reproducibility is quite good.

Moreover, we cannot simultaneously reproduce SP00's two curves with the same set of $\ell_{\rm p}$ values, even when including the forbidden values. One explanation may be that SP00 used $\ell_{\rm p}$

[13] In SP00, the coefficient of 4.18 quoted in their Equation (14) should be 4.82, owing to a typo.

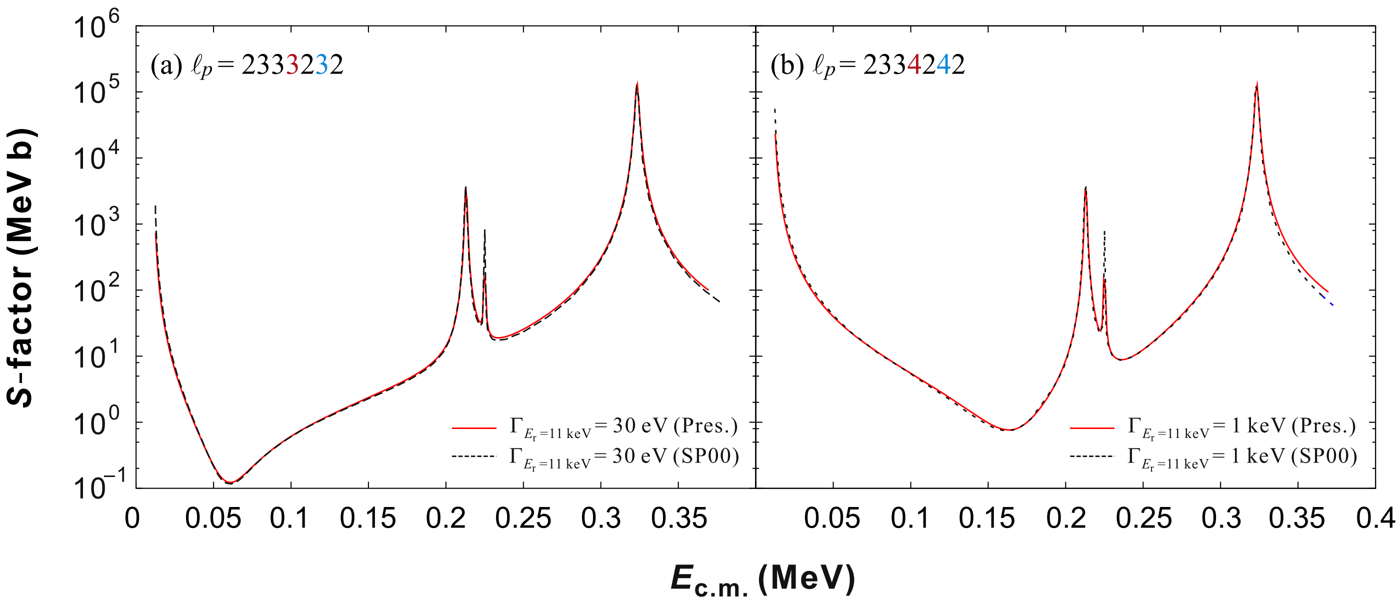

Figure 12. Reproduction of Figure 6 of SP00. Contributions of the 11 keV resonance and its interference effect with the 323 keV resonance are calculated, (a) for the $\Gamma_{E_r=11} = 30$ eV case, and (b) for the $\Gamma_{E_r=11} = 1$ keV case, respectively. Here, seven numbers indicate the ℓ_p values adopted for the seven resonances as listed in Table 5, where the fourth and sixth numbers are for the 323 keV and 564 keV resonances, respectively. The present fits are shown by the solid lines, and the previous ones by the dotted lines.

Table 5
Parameters for the Seven Resonances Listed in Table 1 of SP00

E_x [a]	E_r^{lab} [b]	$E_r^{c.m.}$ [c]	J^π [d]	allowed ℓ_p
12855[e]	11.6	11.0	1^+	0 or 2
13060.7	224.99	212.71	2^-	1 or 3
13073[f]	237.0	225.15	3^-	3
13171.3	340.46	323.31	1^+	0 or 2
13307.5	483.91	459.53	1^+	0 or 2
13414	594.4	564.42	2^-	1 or 3
13484	669.0	635.31	1^+	0 or 2

Notes. Here, the allowed ℓ_p values for each resonance are listed in the last column. All energies are in units of keV.
[a] Taken from Tilley et al. (1998), unless otherwise specified;
[b] Taken from Table 1 of SP00;
[c] Taken from NACRE (same as those in our Table 1), unless otherwise specified;
[d] Taken from NACRE;
[e] Taken from SP00 based on the experiment of Kious (1990);
[f] First observed by SP00.

values as free parameters instead of considering the angular momentum conservation law. Based on our reproducibility of the previous curves, this explanation seems reasonable. The planned direct measurement of the $^{19}F(p,\alpha_\gamma)^{16}O$ channel at JUNA will ultimately explain this discrepancy.

Appendix B
About Acronyms Used in the Text

Throughout the text and figures, for simplicity we have used many acronyms, which represent the references listed in the following Table 6.

Table 6
Acronyms and the Corresponding References Used in the Text.

Acronym	Reference
WI52	Willard et al. (1952)
RA58	Ranken et al. (1958)
CU80	Cuzzocrea et al. (1980)
BE82	Becker et al. (1982)
CF88	Caughlan & Fowler (1988)
CR91	Croft (1991)
ZA95a	Zahnow et al. (1995)
SP97	Spyrou et al. (1997)
SP00	Spyrou et al. (2000)
IN17	Indelicato et al. (2017)
NACRE	Angulo et al. (1999)

ORCID iDs

L. Y. Zhang https://orcid.org/0000-0002-4047-7677
A. I. Karakas https://orcid.org/0000-0002-3625-6951

References

Abia, C., Cunha, K., Cristallo, S., et al. 2011, ApJL, 737, L8
Abia, C., Cunha, K., Cristallo, S., & de Laverny, P. 2015, A&A, 581, A88
Ajzenberg-Selove, F. 1987, NuPhA, 475, 1
Angulo, C., Arnould, M., Rayet, M., et al. 1999, NuPhA, 656, 3
Ask, L. 1965, Ark. Phys., 29, 196
Asplund, M., Grevesse, M., Sauval, A. J., & Scott, P. 2009, ARA&A, 47, 481
Bahcall, N. A., & Fowler, W. A. 1969, ApJ, 157, 645
Becker, H. W., Kieser, W. E., Rolfs, C., Trautvetter, H. P., & Wiescher, M. 1982, ZPhyA, 305, 319
Betts, R. R., Fortune, H. T., & Middleton, R. 1975, PhRvC, 11, 19
Blatt, J. M., & Weisskopf, V. F. 2010, Theoretical Nuclear Physics (New York: Dover Pub.)

Bonner, T. W., & Evans, J. E. 1948, PhRv, 73, 666
Bonner, T. W., Kraus, A. A., Marion, J. B., & Schiffer, J. P. 1956, PhRv, 102, 1348
Busso, M., Palmerini, S., Maiorca, E., et al. 2010, ApJL, 717, L47
Busso, M., Wasserburg, G. J., Nollett, K. M., & Calandra, A. 2007, ApJ, 671, 802
Caughlan, G. R., & Fowler, W. A. 1988, At. Data Nucl. Data Tables, 40, 28
Chao, C. Y., Tollestrup, A. V., Fowler, W. A., & Lauritsen, C. C. 1950, PhRv, 80, 1035
Clayton, G. C., Geballe, T. R., Herwig, F., Fryer, C., & Asplund, M. 2007, ApJ, 662, 1220
Cristallo, S., Straniero, O., Gallino, R., et al. 2009, ApJ, 696, 797
Croft, S. 1991, NIMPA, 307, 353
Cuzzocrea, P., De Rosa, A., Inglima, G., et al. 1980, Lett. Nuovo Cim., 28, 515
Cyburt, R. H., Amthor, A. M., Ferguson, R., et al. 2010, ApJS, 189, 240
Grisoni, V., Romano, D., Spitoni, E., et al. 2020, MNRAS, 498, 1252
He, J. J., Lombardo, I., Dell'Aquila, et al. 2018, ChPhC, 42, 015001
He, J. J., Xu, S. W., Ma, S. B., et al. 2016, SCPMA, 59, 652001
Herwig, F., Bloecker, T., Schoenberner, D., & El Eid, M. 1997, A&A, 324, L81
Indelicato, I., La Cognata, M., Spitaleri, C., et al. 2017, ApJ, 845, 19
Jorissen, A., Smith, V. V., & Lambert, D. L. 1992, A&A, 261, 164
Karakas, A. I. 2010, MNRAS, 403, 1413
Karakas, A. I. 2014, MNRAS, 445, 347
Kious, M. 1990, PhD thesis, Universite de Paris XI
La Cognata, M., Mukhamedzhanov, A. M., Spitaleri, C., et al. 2011, ApJL, 739, L54
La Cognata, M., Palmerini, S., Spitaleri, C., et al. 2015, ApJ, 805, 128
Lam, Y. H., He, J. J., Parikh, A., et al. 2016, ApJ, 818, 78
Liu, W. P., Li, Z. H., He, J. J., et al. 2016, SCPMA, 59, 642001
Lombardo, I., Dell'Aquila, D., Di Leva, A., et al. 2015, PhLB, 748, 178
Lombardo, I., Dell'Aquila, D., He, J. J., Spadaccini, G., & Vigilante, M. 2019, PhRvC, 100, 044307
Longland, R., Iliadis, C., Champagne, A. E., et al. 2010, NuPhA, 841, 1
Lorentz-Wirzba, H. 1978, PhD thesis, Univ. Müster
Lucatello, S., Masseron, T., Johnson, J. A., Pignatari, M., & Herwig, F. 2011, ApJ, 729, 40
Lugaro, M., Karakas, A. I., Bruno, C. G., et al. 2017, NatAs, 1, 0027
Lugaro, M., Ugalde, C., Karakas, A. I., et al. 2004, ApJ, 615, 934
Meynet, G., & Arnould, M. 2000, A&A, 355, 176
Nollett, K. M., Busso, M., & Wasserburg, G. J. 2003, ApJ, 582, 1036
Nucci, M. C., & Busso, M. 2014, ApJ, 787, 141
Palmerini, S., D'Agata, G., La Cognata, M., et al. 2019, JPhCS, 1308, 012016
Palmerini, S., Trippella, O., & Busso, M. 2017, MNRAS, 467, 1193
Pandey, G., Lambert, D. L., & Kameswara, R. N. 2008, ApJ, 674, 1068
Ranken, W. A., Bonner, T. W., & McCrary, J. H. 1958, PhRv, 109, 1646
Rauscher, T., Heger, A., Hoffman, R. D., & Woosley, S. E. 2002, ApJ, 576, 323
Rauscher, T., & Thielemann, F.-K. 2000, ADNDT, 75, 1
Rolfs, C. E., & Rodney, W. S. 1988, Cauldrons in the Cosmos (Chicago: Univ. of Chicago Press)
Ryde, N., Jönsson, H., Mace, G., et al. 2020, ApJ, 893, 37
Schatz, H., Bertulani, C. A., Brown, B. A., et al. 2005, PhRvC, 72, 065804
Sergi, M. L., Spitaleri, C., La Cognata, M., et al. 2010, PhRvC, 82, 032801R
Spyrou, K., Chronidou, C., Harissopulos, S., Kossionides, S., & Paradellis, T. 1997, ZPhyA, 357, 283
Spyrou, K., Chronidou, C., Harissopulos, S., et al. 2000, EPJA, 7, 79
Tarasov, O. B., & Bazin, D. 2004, NuPhA, 746, 411c
Tilley, D. R., Cheves, C. M., Kelley, J. H., Raman, S., & Weller, H. R. 1998, NuPhA, 636, 249
Wang, M., Audi, G., Kondev, F. G., et al. 2017, ChPhC, 41, 030003
Wiescher, M., Görres, J., & Schatz, H. 1999, JPhG, 25, R133
Willard, H. B., Bair, J. K., Kington, J. D., et al. 1952, PhRv, 42, 849
Woosley, S. E., & Haxton, W. C. 1988, Natur, 334, 45
Zahnow, D., Angulo, C., Rolfs, C., et al. 1995, ZPhyA, 351, 229
Zhang, L. Y., Xu, S., He, J., et al. 2019, NIMPB, 438, 48